

# Two-dimensional $P\bar{3}m1$ $\text{Ca}_3\text{N}_2$ , $\text{Ba}_3\text{P}_2$ , and $\text{Ba}_3\text{As}_2$ : Promising stable narrow-gap semiconductors for infrared and broadband photodetectors

Qing-Yuan Chen<sup>✉</sup>, Fei-Jie Huang, Ju-Qi Ruan, Yi-Fen Zhao, and Xiong-Fei Zhang  
*School of Physical Science and Technology, Kunming University, Kunming 650214, China*

Kai Xiong<sup>✉</sup>

*Materials Genome Institute, School of Materials and Energy, Yunnan University, Kunming 650091, China*

Yao He

*Department of Physics, Yunnan University, No.2 Green Lake North Road, Wu Hua Qu, Kunming, Yunnan Province 650091, China*

(CLEO Collaboration)



(Received 9 May 2024; revised 4 August 2024; accepted 23 August 2024; published 5 September 2024)

Exploring two-dimensional (2D) narrow-gap materials with exceptional stability and outstanding photoelectric performance has become a key focus in nano-optoelectronics. However, most existing 2D materials contain relatively large band gaps, and those with narrow band gaps tend to have inadequate stability. This study employed first-principles calculation to predict three alternative narrow-gap 2D binary group ( $\text{II}_3\text{-V}_2$ ) materials in the  $P\bar{3}m1$  space group:  $\text{Ca}_3\text{N}_2$ ,  $\text{Ba}_3\text{P}_2$ , and  $\text{Ba}_3\text{As}_2$ . All these materials exhibit excellent energetic, mechanical, dynamic, and thermal stability. Their mechanical properties reveal isotropic characteristics and demonstrate excellent in-plane stiffness and flexibility. Regarding electronic properties, monolayer  $\text{Ca}_3\text{N}_2$ ,  $\text{Ba}_3\text{P}_2$ , and  $\text{Ba}_3\text{As}_2$  possess indirect narrow band gaps of 0.41, 0.61, and 0.68 eV, respectively. Moreover, they exhibit high electron mobilities (about  $10^3\text{--}10^4 \text{ cm}^2 \text{ V}^{-1} \text{ s}^{-1}$ ) and are nearly isotropic. In terms of optical properties, they demonstrate a significantly broad absorption range, spanning from the IR to visible and UV regions, with remarkably high absorption coefficients (approximately  $10^4\text{--}10^5 \text{ cm}^{-1}$ ). Additionally, their exciton binding energies are higher than those observed in traditional bulk materials while lower than most other 2D materials, facilitating excellent light-driven performance. We propose that these alternative 2D  $P\bar{3}m1$   $\text{Ca}_3\text{N}_2$ ,  $\text{Ba}_3\text{P}_2$ , and  $\text{Ba}_3\text{As}_2$  binary narrow-gap semiconductors will hold promising application prospects in nano-optoelectronic fields such as IR light detection, ambipolar transistors, medical imaging, electrodes, optical communication, and remote sensing.

DOI: 10.1103/PhysRevApplied.22.034013

## I. INTRODUCTION

Narrow-gap materials have become highly relevant in modern optoelectronic fields such as medical imaging, optical communication, security surveillance, remote sensing, gas detection, the modern Internet of Things, photovoltaics, water purification, electrodes, photosensitivity, and photodetection [1–9]. The keys are that narrow-gap materials own an extensive light-absorption range and exceptional infrared (IR) detection performance. Currently, the majority of the reported narrow-gap semiconductors are bulk materials, primarily including II-VI and III-V group materials, such as  $\text{Hg}_x\text{Cd}_{1-x}\text{Te}$ , indium gallium arsenide  $\text{In}_x\text{Ga}_{1-x}\text{As}$  or  $\text{InSb}$ , gallium

arsenide/aluminum gallium arsenide [ $\text{GaAs}/(\text{Al}, \text{Ga})\text{As}$ ] quantum well, indium arsenide antimony/aluminum arsenide antimony [ $(\text{In}, \text{As})\text{Sb}/(\text{Al}, \text{As})\text{Sb}$ ] superlattice, as well as type-II InAs/GaSb superlattices [1,10–15]. However, these materials suffer from drawbacks such as complicated fabrication processes, volume-dependent thermal noise, and limited pixel size [1,16–19]. Any of these limitations restrict further applications of these narrow-gap semiconductor bulk materials.

With continuous development in recent years, 2D materials have emerged as highly promising candidates for numerous optoelectronic applications [20–25]. Compared to traditional bulk narrow band-gap materials, 2D narrow-gap semiconductors offer a range of advantages such as small size, relatively simple preparation processes, high-quality surfaces without dangling bonds,

\*Contact author: qingyuanchen212@163.com

strong light-matter interaction, a broad range of photodetection, high photoresponse rates, good flexibility, ease in constructing heterostructures, excellent mechanical properties, and good compatibility with CMOS devices [1,26–30]. These unique advantages can address the shortcomings of traditional bulk narrow-gap materials, making 2D narrow-gap semiconductors a crucial research focus in modern optoelectronics, particularly in IR detection and applications requiring a broad range of photoresponse [1,26–30]. As research in relevant fields continues to progress, an increasing number of 2D narrow-gap materials have been discovered by researchers, including graphene, transition metal dichalcogenides (TMDs, such as MoS<sub>2</sub>, MoTe<sub>2</sub>, WSe<sub>2</sub>, and WS<sub>2</sub>), black phosphorus with black arsenic phosphorus (b-As<sub>x</sub>P<sub>1-x</sub>), black phosphorus (bP), tellurium (Te), noble metal dichalcogenides (e.g., PtSe<sub>2</sub> and PdSe<sub>2</sub>), and XP<sub>2</sub> ( $X = \text{Ni, Pd, Pt}$ ) [1,14,15, 31–33]. Despite their enormous potential, 2D narrow-gap semiconductors still exhibit several limitations in practical applications, and only a limited number of 2D narrow-gap semiconductors have been successfully applied in relevant fields. For instance, graphene has a low intrinsic sensitivity (less than tens of mAW<sup>-1</sup>), TMDs possess huge band gaps, and few-layer black phosphorus is unstable in ambient air conditions and challenging to produce on a large scale [1,14,15,31,32]. Consequently, researchers are dedicated to exploring alternative 2D narrow-gap semiconductor materials with excellent stability and superior optoelectronic performance.

Recent studies have revealed a promising class of 2D materials composed of group IIA and VA elements, denoted as II<sub>x</sub>V<sub>y</sub> [34–40]. Among these, compounds with a 3:2 stoichiometry, specifically II<sub>3</sub>V<sub>2</sub>, have garnered significant interest due to their notable structural stability and remarkable optoelectronic properties. These compounds hold considerable promise for applications within energy and optoelectronics. For instance, the electron mobility of Sr<sub>3</sub>P<sub>2</sub> can reach up to  $2.46 \times 10^4 \text{ cm}^2 \text{ V}^{-1} \text{ s}^{-1}$ , while the photoelectric conversion efficiency of Ca<sub>3</sub>P<sub>2</sub>/AlN heterojunctions is as high as 21.1% [35]. Nevertheless, the currently discovered II<sub>3</sub>V<sub>2</sub> compound 2D materials generally have large band gaps (greater than 1 eV), which constrains their utility in IR detection and applications requiring a wide range of photoresponse where narrow-gap 2D materials are highly desired [34–40]. As such, exploring II<sub>3</sub>V<sub>2</sub> compounds is imperative, focusing on those with narrow band gaps, excellent stability, and superior optoelectronic properties to fully exploit their potential in relevant fields.

Herein, using computational materials screening and state-of-the-art first-principles calculations based on the density-functional theory (DFT), we predict three alternative monolayer group II-V compounds in a 3 : 2 ratio, namely Ca<sub>3</sub>N<sub>2</sub>, Ba<sub>3</sub>P<sub>2</sub>, and Ba<sub>3</sub>As<sub>2</sub>. These materials belong to the  $P\bar{3}m1$  space group. By calculating total

energy, elastic constants, phonon band dispersion, and *ab initio* molecular dynamics (AIMD), we verified that these three alternative monolayer II<sub>3</sub>V<sub>2</sub> possess excellent energetic, mechanical, dynamic, and thermodynamic stability. Subsequently, we systematically studied their mechanical, electronic, and optical properties. Our research findings reveal that, in contrast to reported narrow-gap semiconductors, the 2D  $P\bar{3}m1$  Ca<sub>3</sub>N<sub>2</sub>, Ba<sub>3</sub>P<sub>2</sub>, and Ba<sub>3</sub>As<sub>2</sub> enrich the family of narrow-gap 2D materials by presenting a suite of distinctive benefits. Notably, unlike the traditional bulk narrow-gap materials, these three 2D materials possess the typical advantages of 2D narrow-gap materials, such as small size, a broad range of photodetection, good flexibility, and excellent mechanical properties. Moreover, when compared with other reported 2D narrow-gap semiconductors like graphene, TMDs, black phosphorus, black phosphorus with black arsenic phosphorus (b-As<sub>x</sub>P<sub>1-x</sub>), and noble metal dichalcogenides, these three 2D materials stand out with ideal narrow band-gap values, high carrier mobilities, exceptional stability, environmentally friendly, and more cost effective to produce, positioning them as promising candidates in the fields of IR light detection and broad-spectrum photoresponsive optoelectronic materials.

## II. METHOD

In the present study, we conducted our computational analyses employing the Vienna *ab initio* simulation package (VASP) [41,42]. This work utilized the projector-augmented wave method [42,43] to meticulously model the interactions among electrons, selecting a plane-wave energy cutoff of 600 eV to ensure the precision of our calculations. To address the exchange-correlation energy, we adopted the generalized gradient approximation formulated by Perdew, Burke, and Ernzerhof (GGA PBE) [41,44]. To further enhance the accuracy of our results, the HSE06 hybrid functional method was employed, a choice motivated by its renowned precision in assessing the electronic and optical properties of materials [45,46]. Our study meticulously configured the Brillouin zone sampling using  $\Gamma$ -centered  $K$  points with a grid resolution of  $18 \times 18 \times 1$ . For structural optimization, the energy convergence and force convergence criteria were stringently set to  $10^{-8}$  eV and 0.01 eV/Å, respectively. To effectively negate interlayer interactions in our monolayer II<sub>3</sub>V<sub>2</sub> structural model, a vacuum layer of 30 Å was introduced orthogonally to the material layers. Given the significant role of *d* electrons in II<sub>3</sub>V<sub>2</sub>, our analysis incorporated comparative calculations both with and without the inclusion of spin-orbital coupling (SOC) in the band-structure evaluations. To account for electron-hole interactions rigorously, we engaged the quasiparticle many-body G<sub>0</sub>W<sub>0</sub> approximation in conjunction with the Bethe Salpeter equation (BSE) for our optical response calculations [47,48]. Computational constraints necessitated a reduction in  $K$ -point

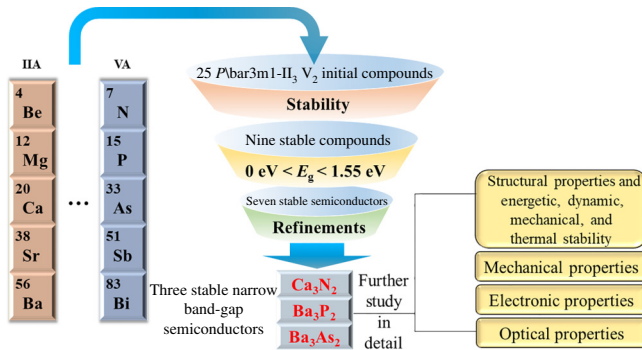


FIG. 1. The screening flowchart of group II-V binary compounds.

sampling to  $9 \times 9 \times 1$  for  $G_0W_0$  calculations, with a corresponding adjustment of the plane-wave cutoff energy to 600 eV. Moreover, the total number of bands considered in the  $G_0W_0$  calculations was expanded to 240 to ensure a comprehensive analysis. The phonon-dispersion curves, essential for understanding the lattice dynamics, were derived using the finite-displacement method facilitated by the PHONOPY code [49]. For the *ab initio* molecular dynamics (AIMD) simulations, we configured a system comprising 80 atoms within a  $4 \times 4 \times 1$  supercell. These simulations were executed throughout 10 ps with a 2-fs timestep, maintaining the thermostat temperature at 600 K to ascertain the thermal stability of the material under study. The QUANTUM ESPRESSO package was utilized to calculate the band symmetry of monolayer  $\text{II}_3\text{V}_2$  [50].

### III. RESULTS AND DISCUSSION

We employed the computational materials' screening approach to study the structural stability and electronic properties of alternative monolayer group II-V binary compounds  $\text{II}_3\text{V}_2$  (where II = Be, Mg, Ca, Sr, and Ba; V = N, P, As, Sb, and Bi) (Fig. 1). The research aimed at pinpointing materials ideally suited for IR optoelectronics applications, particularly within the wavelength spectrum of 0.8–30  $\mu\text{m}$ . This objective necessitated materials possessing a band gap inferior to 1.55 eV. Initially, we evaluated 25 2D  $P\bar{3}m1$   $\text{II}_3\text{V}_2$  materials, identifying nine with confirmed mechanical, dynamic, and thermal stability (see Table I). A subsequent refinement using electronic property criteria yielded a subset of seven materials with semiconductive properties. Following this, we eliminated previously explored compounds, specifically  $\text{Ca}_3\text{P}_2$ ,  $\text{Ca}_3\text{As}_2$ ,  $\text{Sr}_3\text{P}_2$ , and  $\text{Sr}_3\text{As}_2$  [35]. Concluding, our comprehensive analysis identified three 2D materials—monolayer  $\text{Ca}_3\text{N}_2$ ,  $\text{Ba}_3\text{P}_2$ , and  $\text{Ba}_3\text{As}_2$ —as fulfilling the outlined criteria, exhibiting admirable stability and narrow-gap semiconducting characteristics. Future stages of our investigation will methodically explore the structural

TABLE I. Band gaps of nine monolayer  $P\bar{3}m1$   $\text{II}_3\text{V}_2$  with mechanical, dynamic, and thermal stability.

Material	Band gap (eV)		
	PBE	PBE+SOC	HSE06
$\text{Mg}_3\text{N}_2$	0.00	0.00	0.00
$\text{Ca}_3\text{N}_2$	0.00	0.00	0.41
$\text{Ca}_3\text{P}_2$	0.94	0.94	1.41
$\text{Ca}_3\text{As}_2$	0.91	0.90	1.38
$\text{Sr}_3\text{N}_2$	0.00	0.00	0.00
$\text{Sr}_3\text{P}_2$	0.58	0.59	1.01
$\text{Sr}_3\text{As}_2$	0.57	0.56	0.99
$\text{Ba}_3\text{P}_2$	0.30	0.29	0.61
$\text{Ba}_3\text{As}_2$	0.35	0.34	0.68

stability alongside the mechanical, electronic, and optical properties of these three promising materials.

### A. Structure characterization

The primary concern with the designed class of materials is their structural properties. Figures 2(a)–2(d) shows the structural schematic diagrams of the alternative monolayer  $\text{II}_3\text{V}_2$  materials in the  $P\bar{3}m1$  space group, including  $\text{Ca}_3\text{N}_2$ ,  $\text{Ba}_3\text{P}_2$ , and  $\text{Ba}_3\text{As}_2$ , from various perspectives. Each material's hexagonal primitive cell is indicated within the black frame, containing three group-II atoms and two group-V atoms, with lattice vectors  $\mathbf{a}$  and  $\mathbf{b}$  being equal and lattice angles  $\alpha = \beta = 90^\circ$  and  $\gamma = 120^\circ$ . Figure 2(d) shows the orthogonal supercell structure, enclosed within the green frame, containing six group-II atoms and four group-V atoms, which visually represents carrier conduction along the  $\mathbf{x}$  and  $\mathbf{y}$  directions. Figures 2(e) and 2(f) correspond to the first Brillouin zone (FBZ) of the primitive cell and the orthogonal supercell, respectively, associated with the hexagonal and orthogonal lattices. From the symmetry perspective, the three materials belong to the  $P\bar{3}m1$  space group, which pertains to the hexagonal system. Due to the high degree of hexagonal symmetry, these three materials should exhibit good stability. We will then conduct an in-depth investigation of the stability of these three materials from various angles.

We conducted a study on the energetic stability of various materials by calculating their binding energy using Eq. (1):

$$E_{\text{coh}} = \frac{3E_{\text{II}}^{\text{atom}} + 2E_{\text{V}}^{\text{atom}} - E_{\text{II}_3\text{V}_2}}{5}, \quad (1)$$

where  $E_{\text{II}}^{\text{atom}}$  and  $E_{\text{V}}^{\text{atom}}$  are the energies of the II atom and V atom, respectively, and  $E_{\text{II}_3\text{V}_2}$  represents the total energy of monolayer  $\text{II}_3\text{V}_2$ . Our findings are presented in Table II. Using the same method, we determined the binding energy of graphene to be 7.95 eV/atom, silicene to be 3.71 eV/atom, and phosphorene to be 3.24 eV/atom [51]. When comparing the results in Table II, we noticed

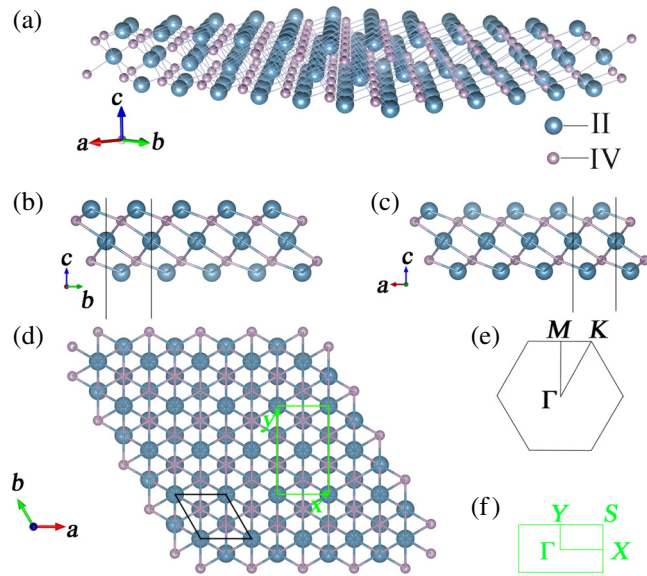


FIG. 2. Panels (a)–(d) are the crystal-structure schematic diagrams of the alternative monolayer  $\text{II}_3\text{V}_2$  materials in the  $P\bar{3}m1$  space group. The primitive cell and the orthogonal supercell are denoted by black and green lines, respectively. (e),(f) correspond to the first Brillouin zone (FBZ) of the primitive cell and the orthogonal supercell, respectively.

that the cohesive energy of  $\text{Ca}_3\text{N}_2$ ,  $\text{Ba}_3\text{P}_2$ , and  $\text{Ba}_3\text{As}_2$  falls within a reasonable range, indicating that these materials have good energetic stability [52]. The mechanical stability of monolayer  $\text{II}_3\text{V}_2$  is determined using the Born-Huang elastic stability criterion, which includes three conditions for material to possess good mechanical stability: (i)  $C_{11} > 0$ , (ii)  $C_{66} > 0$ , and (iii)  $C_{11}C_{22} - C_{12}^2 > 0$ .  $C_{ij}$  represents the second-order in-plane elastic constant calculated using the energy-strain method [53]. The calculation of  $C_{ij}$  is based on the following equation:  $C_{ij} = (1/S_0) (\partial E / \partial \varepsilon_i \partial \varepsilon_j)$ , where  $S_0$  represents the equilibrium area of the system,  $E$  represents the strain energy, and  $\varepsilon_{ij}$  denotes the corresponding in-plane strains ranging from  $-1.5\%$  to  $1.5\%$ , with an interval of  $0.5\%$ . The results of the calculations are presented in Table III, and we found that  $\text{Ca}_3\text{N}_2$ ,  $\text{Ba}_3\text{P}_2$ , and  $\text{Ba}_3\text{As}_2$  all possess mechanical stability.

Figure 3 depicts these materials' phonon dispersion curves and phonon density of states (PhDOS). The lack of imaginary frequencies across the entire Brillouin zone

signifies  $\text{Ca}_3\text{N}_2$ ,  $\text{Ba}_3\text{P}_2$ , and  $\text{Ba}_3\text{As}_2$  hold remarkable dynamic stability. The peak phonon frequencies identified are as follows: for  $\text{Ca}_3\text{N}_2$ , 12.35 THz ( $411.95\text{ cm}^{-1}$ ); for  $\text{Ba}_3\text{P}_2$ , 6.09 THz ( $203.14\text{ cm}^{-1}$ ); and for  $\text{Ba}_3\text{As}_2$ , 4.14 THz ( $138.10\text{ cm}^{-1}$ ). These findings imply a substantial bond network within the  $\text{Ca}_3\text{N}_2$ ,  $\text{Ba}_3\text{P}_2$ , and  $\text{Ba}_3\text{As}_2$  monolayers. Further scrutiny of the dynamic characteristics of these materials was undertaken by examining the PhDOS plots (referenced as Fig. 3). It is clear that the phonon-vibration frequencies of monolayer  $\text{II}_3\text{V}_2$  predominantly concentrate in three discrete ranges interspersed with two phonon band gaps. For example, in  $\text{Ca}_3\text{N}_2$ , the vibration frequencies primarily span the low-frequency range (0–6.18 THz), the midfrequency range (6.33–7.42 THz), and the high-frequency range (9.36–12.39 THz), with two phonon gaps evident.  $\text{Ba}_3\text{P}_2$ , and  $\text{Ba}_3\text{As}_2$  display analogous patterns, wherein their vibration frequencies concentrate in specific ranges accompanied by phonon gaps. The analysis reveals that the high-frequency phonons are principally attributed to the vibrations of V atoms, with a minor contribution from II atoms, thus affirming the robust II-V bond interactions in monolayer  $\text{II}_3\text{V}_2$ . In the midfrequency range, the vibrations predominantly originate from II atoms, whereas in the low-frequency range, contributions arise from both II atoms and a limited number of V atoms. Notably, the vibration frequencies and phonon gaps in monolayer  $\text{II}_3\text{V}_2$  exhibit variability with respect to the composition of the materials. Specifically, a transition from N to As in the group-V atom or from Ca to Ba in the group-II atom reduces the maximum phonon frequency. Concurrently, the phonon gap in the higher-frequency range decreases, whereas the gap in the lower-frequency range increases. Essentially, the phonon vibration frequency range and the phonon gaps in monolayer  $\text{II}_3\text{V}_2$  are adjustable through atom and alloy engineering. Additionally, the phonon band gap within these materials acts as a prohibitive barrier to the propagation of mechanical waves within specific frequency ranges, rendering monolayer  $\text{II}_3\text{V}_2$  a promising candidate for applications in phononic devices, such as phonon waveguides, cavities, and filters, etc.

To assess the practical application potential of 2D  $\text{II}_3\text{V}_2$ , we employed *ab initio* molecular dynamics simulations (AIMDs) to investigate their thermal stability at an elevated temperature of 600 K throughout 10 ps. Our analysis, focusing on their total energy and structural integrity

TABLE II. Optimized lattice parameters, cohesive energy, and band gap of monolayer  $\text{II}_3\text{V}_2$ .

Material	$\mathbf{a} = \mathbf{b}$ (Å)	$\alpha = \beta$ (deg)	$\gamma$ (deg)	Cohesive energy (eV/atom)	Band gap (eV)		
					PBE	PBE+SOC	HSE06
$\text{Ca}_3\text{N}_2$	3.691	90	120	3.89	0.00	0.00	0.41
$\text{Ba}_3\text{P}_2$	4.811	90	120	3.39	0.30	0.29	0.61
$\text{Ba}_3\text{As}_2$	4.955	90	120	3.24	0.35	0.34	0.68

TABLE III. The elastic constants [ $C_{ij}$  (N/m)], Young's modulus [ $Y^{2D}(\theta)$  (N/m)] and Poisson's ratios ( $\nu(\theta)$ ) of monolayer  $\text{II}_3\text{V}_2$ .

Material	$C_{11}$	$C_{22}$	$C_{12}$	$C_{66}$	$Y^{2D}_{\max}(\theta)$	$Y^{2D}_{\min}(\theta)$	$\nu_{\max}(\theta)$	$\nu_{\min}(\theta)$
$\text{Ca}_3\text{N}_2$	85.269	85.269	29.761	27.754	74.882	74.882	0.349	0.349
$\text{Ba}_3\text{P}_2$	35.635	35.635	6.240	14.698	34.543	34.543	0.175	0.175
$\text{Ba}_3\text{As}_2$	32.276	32.276	5.452	13.412	31.355	31.355	0.169	0.169

(Fig. 4), demonstrated that the  $\text{Ca}_3\text{N}_2$ ,  $\text{Ba}_3\text{P}_2$ , and  $\text{Ba}_3\text{As}_2$  maintained remarkable thermal stability of these 2D materials from room temperature to 600-K environments.

## B. Mechanical characterization

Herein, we aim to discuss the basic mechanical properties of monolayer  $\text{II}_3\text{V}_2$ , including the orientation-dependent Young's modulus and Poisson's ratio, by assessing mechanical constants  $C_{ij}$  obtained in Table III. The calculation process adopts the following equations [54]:

$$Y^{2D}(\theta) = \frac{C_{11}C_{22} - C_{12}^2}{C_{11}s^4 + C_{22}c^4 + \left( \frac{C_{11}C_{22} - C_{12}^2}{C_{66}} - 2C_{12} \right)s^2c^2}, \quad (2)$$

$$\nu(\theta) = \frac{C_{12}(s^4 + c^4) - \left( C_{11} + C_{22} - \frac{C_{11}C_{22} - C_{12}^2}{C_{66}} \right)s^2c^2}{C_{11}s^4 + C_{22}c^4 + \left( \frac{C_{11}C_{22} - C_{12}^2}{C_{66}} - 2C_{12} \right)s^2c^2}, \quad (3)$$

where  $s = \sin \theta$ , and  $c = \cos \theta$ ,  $\theta$  ranges from 0 to  $2\pi$ , as depicted in Fig. 5 and Table III. Results revealed that the values of Young's modulus and Poisson's ratio of the three materials,  $\text{Ca}_3\text{N}_2$ ,  $\text{Ba}_3\text{P}_2$ , and  $\text{Ba}_3\text{As}_2$ , exhibit a descending order. Additionally, we observed that for each material, Young's modulus and Poisson's ratio show equal values along different orientations. Our findings demonstrate that monolayer  $\text{II}_3\text{V}_2$  are 2D materials with exceptional in-plane isotropic mechanical attributes.

To validate in-plane stiffness and flexibility, we studied the ultimate tensile strain of these materials [55]. This

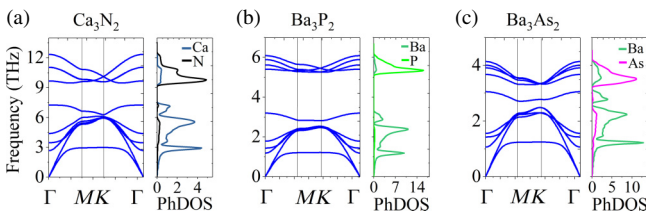


FIG. 3. (a)–(c) The phonon-dispersion spectrum and the atom-projected phonon density of states (PhDOS) of the monolayer  $\text{II}_3\text{V}_2$ .

property indicates their ability to withstand significant tensile strain without failure. We analyzed the stress-strain relationship under axial tensile strain in cubic supercells to investigate the ideal strength of the monolayer  $\text{II}_3\text{V}_2$ . The stress-strain curves for the monolayer  $\text{II}_3\text{V}_2$  compounds are presented in Fig. 6, where the upper limit of strain represents the ultimate tensile strain (UTS) or ideal strength. We separately studied the stress-strain curves under uniaxial strain along the  $x$  and  $y$  axes and under biaxial strain and labeled the corresponding UTS values as  $\text{UTS}_x$ ,  $\text{UTS}_y$ , and  $\text{UTS}_{xy}$ . The strain step size during the calculations was set to 1%. For  $\text{Ca}_3\text{N}_2$ , we observed  $\text{UTS}_x$  of 35%,  $\text{UTS}_y$  of 23%, and  $\text{UTS}_{xy}$  of 13%. For  $\text{Ba}_3\text{P}_2$ , the values were  $\text{UTS}_x$  of 23%,  $\text{UTS}_y$  of 14%, and  $\text{UTS}_{xy}$  of 8%. Moreover, for  $\text{Ba}_3\text{As}_2$ , the  $\text{UTS}_x$  was 21%,  $\text{UTS}_y$  was 9%, and  $\text{UTS}_{xy}$  was 7%. In all three materials, a consistent trend of  $\text{UTS}_x > \text{UTS}_y > \text{UTS}_{xy}$  is observed. The reported maximum uniaxial UTS values of graphene and hexagonal boron nitride are 27% and 30%. These values are comparable to the UTS values observed in these monolayer  $\text{II}_3\text{V}_2$ , which exhibit ultrahigh ideal strength and good ductility. Thus, the 2D  $\text{II}_3\text{V}_2$  compounds play a significant role in the mechanical properties of 2D materials.

## C. Electronic characterization

In the ensuing discussion, we explore the electronic properties of monolayer  $\text{II}_3\text{V}_2$ . Given that most  $\text{II}_3\text{V}_2$  materials incorporate  $d$  electrons, an initial examination of their band structures should be conducted with and without spin-orbital coupling (SOC), facilitating comparative analysis of their band gaps as delineated in Table II. It is evident that the incorporation of SOC results in a marginal

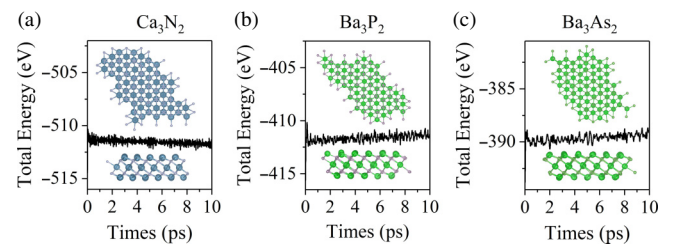


FIG. 4. Total energy of the monolayer  $\text{Ca}_3\text{N}_2$  (a),  $\text{Ba}_3\text{P}_2$  (b), and  $\text{Ba}_3\text{As}_2$  (c) in AIMD simulations at 600 K over 10 ps. The top view and side view of the monolayer  $\text{II}_3\text{V}_2$  supercell at 10 ps are inserted.

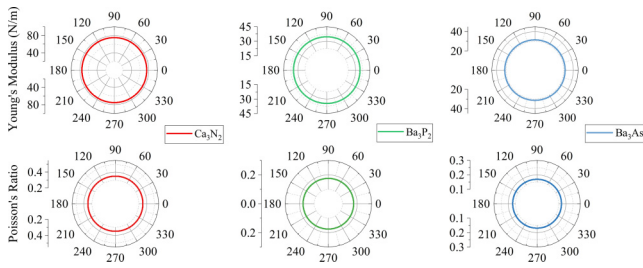


FIG. 5. The orientation-dependent  $Y^{2D}(\theta)$  (N/m) and Poiss. ratios ( $v(\theta)$ ) for monolayer  $\text{II}_3\text{V}_2$ .

diminution of the band gap in the band structures of monolayer  $\text{II}_3\text{V}_2$  proximal to the Fermi level, in contrast to the configurations without SOC. Considering the substantial computational difficulties of this research alongside the minimal influence exerted by SOC on the outcomes, our discussions will predominantly focus on the results obtained without SOC. Furthermore, in pursuit of results that resonate more congruently with experimental findings, the HSE06 hybrid functional method was employed to calculate and elucidate the electronic properties of monolayer  $\text{II}_3\text{V}_2$ .

We now undertake a detailed analysis of the band structures, projected density of states (PDOS), and projected band structures of  $\text{Ca}_3\text{N}_2$ ,  $\text{Ba}_3\text{P}_2$ , and  $\text{Ba}_3\text{As}_2$ , depicted in Figs. 7 and 8, respectively. These figures reveal that each of the three semiconductors falls into the indirect band-gap materials. In particular, their valence-band maximum (VBM) is situated at the high-symmetry  $M$  point, whereas their conduction-band minimum (CBM) is located at the high-symmetry  $\Gamma$  point. Employing the HSE06 computational method, we have ascertained the band-gap values for  $\text{Ca}_3\text{N}_2$ ,  $\text{Ba}_3\text{P}_2$ , and  $\text{Ba}_3\text{As}_2$  to be 0.41, 0.61, and 0.68 eV, respectively. Further, in  $\text{Ca}_3\text{N}_2$ , the VBM predominantly comprises  $\text{N}-p$  electrons, with a minor contribution from  $\text{Ca}-d$  electrons and a negligible presence of  $\text{Ca}-p$  electrons. Similarly, the CBM is mainly constituted of  $\text{N}-p$  and  $\text{Ca}-d$  electrons, with a slight involvement of  $\text{Ca}-p$  electrons. In  $\text{Ba}_3\text{P}_2$ , the VBM is primarily composed of  $\text{P}-p$  electrons, augmented by a modest amount of  $\text{Ba}-d$  electrons and a minimal quantity of  $\text{Ba}-p$  electrons, while the CBM is mainly made up of  $\text{Ba}-d$  electrons. Similar patterns are observed in  $\text{Ba}_3\text{As}_2$ , where the VBM is principally constituted of  $\text{As}-p$  electrons, supplemented by a minor component of  $\text{Ba}-d$  electrons and a trivial portion of  $\text{Ba}-p$  electrons, and the CBM is predominantly composed of  $\text{Ba}-d$  electrons. The  $p-d$  hybridization effect in these materials holds the potential to stabilize the structure at the band edges, influencing the material's band-gap characteristics and contributing to its overall stability and narrow band gap [39].

Furthermore, we conducted a symmetry analysis of the electric dipole transitions in the band structures of  $\text{Ca}_3\text{N}_2$ ,  $\text{Ba}_3\text{P}_2$ , and  $\text{Ba}_3\text{As}_2$ , based on the selection rules for electric dipole transitions from group theory. The results, which include the point groups and irreducible representations at high-symmetry points for dipole transitions from the topmost valence band to the lowest conduction band, are meticulously detailed in Table IV. Our analysis disclosed that for  $\text{Ca}_3\text{N}_2$ , dipole transitions are allowed from the topmost valence band at  $\Gamma$  to the lowest conduction band at  $\Gamma$ , and similarly from  $K$  to  $K$ , while they are forbidden from  $M$  to  $M$ . In comparison,  $\text{Ba}_3\text{P}_2$  and  $\text{Ba}_3\text{As}_2$  demonstrate allowed transitions from the topmost valence band to the lowest conduction band at the high-symmetry points of  $\Gamma$  and  $M$ , while forbidden for the  $K$  to  $K$  in-plane transitions. To validate the transition probabilities between the band edges, we have calculated the squared transition dipole moments ( $\text{TDM}^2$ ), denoted by  $P^2$ , using the HSE06 method at different high-symmetry points [56]. We considered the direct transitions between the topmost valence band and the lowest conduction band, per the approaches outlined in prior research [56,57]. Results reveal that the  $P^2$  for the direct transitions between band edges across the

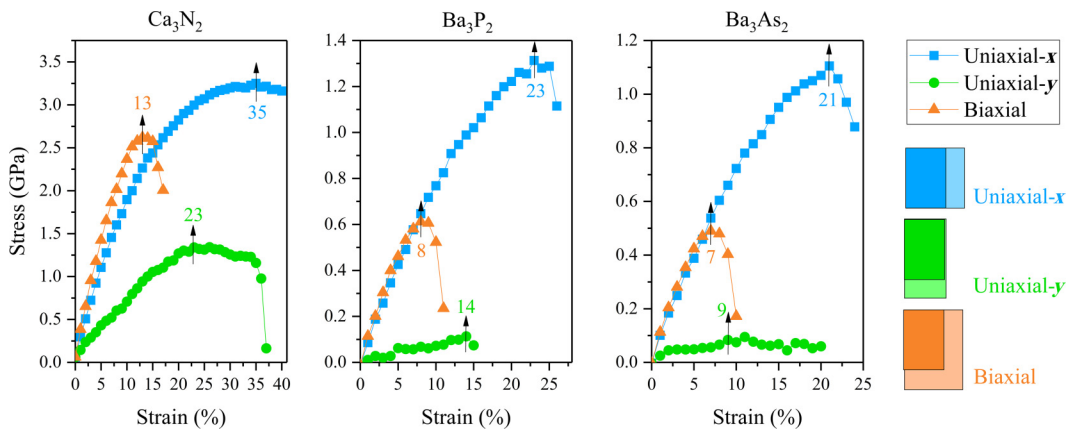


FIG. 6. Stress-strain relationship of monolayer  $\text{II}_3\text{V}_2$  under  $x$ -uniaxial strain (blue),  $y$ -uniaxial strain (green), and biaxial strain (orange). The ultimate tensile strain (or ultimate tensile strength, UTS) points for each considered compound are depicted by an arrow.

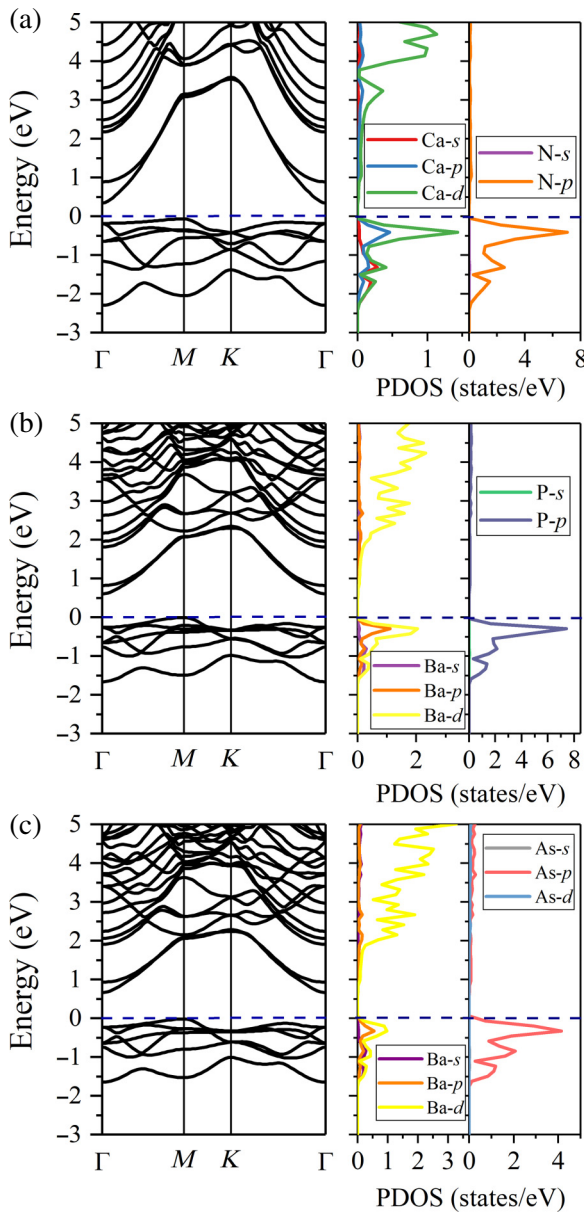


FIG. 7. The band structures and projected density of states (PDOS) of  $\text{Ca}_3\text{N}_2$ ,  $\text{Ba}_3\text{P}_2$  (b), and  $\text{Ba}_3\text{As}_2$  (c) under the HSE06 method.

materials are as follows:  $\text{Ca}_3\text{N}_2$  manifests a  $\Gamma$ - $\Gamma$  transition of 440.13 Debye $^2$ , an  $M$ - $M$  transition of 0.24 Debye $^2$ , and a  $K$ - $K$  transition of 0.32 Debye $^2$ ;  $\text{Ba}_3\text{P}_2$  exhibits a  $\Gamma$ - $\Gamma$  transition of 138.83 Debye $^2$ , an  $M$ - $M$  transition of 15.37 Debye $^2$ , and a  $K$ - $K$  transition of 0.93 Debye $^2$ ; and  $\text{Ba}_3\text{As}_2$  displays a  $\Gamma$ - $\Gamma$  transition of 199.61 Debye $^2$ , an  $M$ - $M$  transition of 10.96 Debye $^2$ , and a  $K$ - $K$  transition of 0.68 Debye $^2$ . Due to biases in our TDM $^2$  calculations,  $P^2$  values lower than 1 Debye $^2$  can be treated as zero. The TDM $^2$  calculations nearly agree with the electric dipole transition results based on the symmetry analysis. It can also be seen that although, in general, the  $K$ - $K$  transition

in  $\text{Ca}_3\text{N}_2$  is permitted based on the symmetry analysis, the TDM $^2$  calculation indicates that it is negligible. These findings underscore the pivotal role of transition intensity in exciton binding energy.

The exciton binding energy, fundamentally rooted in the Coulombic attraction between electrons and holes, is profoundly modulated by the band structure, specifically through the lens of transition intensity. A strong correlation exists between the magnitude of the TDM and the transition intensity of excitons, where robust intensities indicate heightened probabilities of electron-hole interactions. Conversely, transitions with weak intensities suggest reduced opportunities for exciton formation, resulting in diminished binding energies. In addition, the indirect band-gap characteristic, as supported by prior research [58,59], decreases the recombination rate of photoexcited carriers. When electrons return to the valence band, they must emit a phonon. This process requires a certain  $k$ -space distance to travel, which hinders the recombination probability between electrons and holes.

Next, we used the deformation potential (DP) theory-based calculation method to compute the effective masses, electron mobilities, and relaxation times of monolayer  $\text{II}_3\text{V}_2$  along various directions at 300 K [60–63]. The results are presented in Table V. We conducted detailed calculations and employed the following equations:

$$\mu_{2D} = \frac{2e\hbar^3 C}{3k_B T |m^*|^2 E_1^2}, \quad (4)$$

$$\tau = \frac{\mu_{2D} m^*}{e}, \quad (5)$$

$$m^* = \hbar^2 \left[ \frac{\partial^2 E}{\partial k^2} \right]^{-1}, \quad (6)$$

$$C = \left[ \frac{\partial^2 E}{\partial (\Delta a/a_0)^2} \right] S_0^{-1}, \quad (7)$$

$$E_1 = \frac{\partial E_{\text{edge}}}{\partial (\Delta a/a_0)}. \quad (8)$$

In these equations,  $\mu_{2D}$  represents the electron mobility of monolayer  $\text{II}_3\text{V}_2$ ,  $C$  is the elastic constant,  $m^*$  is the effective mass of the carrier,  $E$  is the total energy of the system under uniaxial strain, and  $\tau$  is the relaxation time of the electron,  $T$  represents temperature and is set to 300 K here, and  $k_B$  stands for the Boltzmann constant. As the monolayer  $\text{II}_3\text{V}_2$  structure exhibits low symmetry along the  $x$  and  $y$  directions, we separately considered the uniaxial strain effects along both directions. Additionally,  $e$  represents the charge of an electron,  $E_1$  is the DP constant,  $E_{\text{edge}}$  is the shift of the band edge considering the vacuum level,  $\Delta a$  is the change in lattice parameters relative to the equilibrium lattice constant under strain, and  $a_0$  represents the lattice constant at equilibrium.

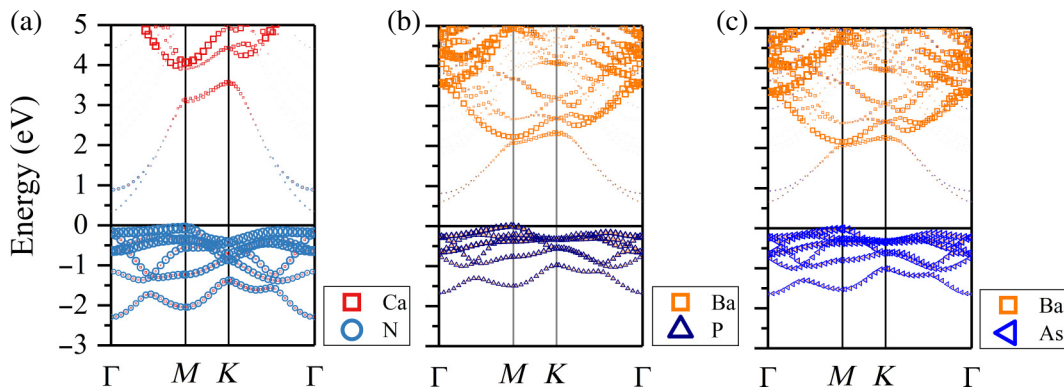


FIG. 8. The projected band structures of monolayer  $\text{Ca}_3\text{N}_2$  (a),  $\text{Ba}_3\text{P}_2$  (b), and  $\text{Ba}_3\text{As}_2$  (c) under the HSE06 method.

The computational analyses reveal that  $\text{Ca}_3\text{N}_2$  demonstrates the electron mobility reaching up to  $3.30 \times 10^3 \text{ cm}^2 \text{ V}^{-1} \text{ s}^{-1}$  along the  $x$  axis and  $3.22 \times 10^3 \text{ cm}^2 \text{ V}^{-1} \text{ s}^{-1}$  along the  $y$  axis. Similarly,  $\text{Ba}_3\text{P}_2$  exhibits electron mobility up to  $3.58 \times 10^3 \text{ cm}^2 \text{ V}^{-1} \text{ s}^{-1}$  in the  $x$  direction and  $3.53 \times 10^3 \text{ cm}^2 \text{ V}^{-1} \text{ s}^{-1}$  in the  $+y$  direction. Notably,  $\text{Ba}_3\text{As}_2$  shows the electron mobility as elevated as  $1.37 \times 10^4 \text{ cm}^2 \text{ V}^{-1} \text{ s}^{-1}$  along the  $x$  direction and  $1.35 \times 10^4 \text{ cm}^2 \text{ V}^{-1} \text{ s}^{-1}$  along the  $y$  direction. Thus,  $\text{II}_3\text{V}_2$  monolayers emerge as another 2D material, featured by its high electron mobility and marginal anisotropy in mobility characteristics. These materials surpass the electron mobility of black phosphorus ( $1000 \text{ cm}^2 \text{ V}^{-1} \text{ s}^{-1}$ ) and potentially rivaling that of graphene. Moreover, from the perspective of relaxation time, the electron relaxation time across different axes can extend to  $10^2$ – $10^3$  femtoseconds at ambient temperature, highlighting the stability of its superior electron transport efficiency and reinforcing its exceptional electrical conductivity.

It should be noted that the DP theory is founded on the scattering process between acoustic phonons and electrons, which tends to overestimate the carrier mobility and relaxation time. Incorporating the effects of optical phonon scattering and possible impurity scattering into computations is essential for a more accurate study of carrier mobility and relaxation time in future studies [64–66].

In short, as potential narrow-gap semiconductors, monolayer  $\text{II}_3\text{V}_2$  compounds manifest extraordinary

electronic properties as another 2D material, heralding these materials can apply in the fields of infrared and the broad range of photoresponse nanosemiconductors and nano-optoelectronic devices.

#### D. Optical characterization

Following, we discuss the optical properties of the materials. We adopted the many-body approach, which combined the quasiparticle (QP) GW method with the Bethe-Salpeter equation (BSE) method [67]. These methods were derived by solving the Bethe-Salpeter equation (BSE), where the quasiparticle (QP) energies and screened interactions (W) were obtained through the GW approximation [67]. The calculated absorption coefficient  $\alpha(\omega)$  for monolayer  $\text{II}_3\text{V}_2$  with in-plane light polarization, using the  $G_0\text{W}_0+\text{BSE}$  calculations, is presented in Fig. 9, where the  $\alpha(\omega)$  was determined using the following equation [68]:

$$\alpha(\omega) = \frac{\sqrt{2}}{c} \omega \left[ \sqrt{\varepsilon_1(\omega)^2 + \varepsilon_2(\omega)^2} - \varepsilon_1(\omega) \right]^{1/2}, \quad (9)$$

where  $\varepsilon_1(\omega)$  and  $\varepsilon_2(\omega)$  represent the real and imaginary parts of the frequency-dependent dielectric function, respectively, and  $c$  is the speed of light. It is worth noting that the calculated absorption coefficients for 2D materials, derived from computing the dielectric function—a common practice in theoretical research—may exhibit slight discrepancies compared to experimentally obtained values.

TABLE IV. The calculated point groups and the respective irreducible representations at high-symmetry points of the valence and conduction band edges for monolayer  $\text{Ca}_3\text{N}_2$ ,  $\text{Ba}_3\text{P}_2$ , and  $\text{Ba}_3\text{As}_2$ .

Material	The topmost valence band								The lowest conduction band		
	$K$ point Point group	$\Gamma$ $D_{3d}$	$M$ $C_{2h}$	$K$ $D_3$	$\Gamma$ $D_{3d}$	$\Gamma$ $D_{3d}$	$M$ $C_{2h}$	$K$ $D_3$	$\Gamma$ $D_{3d}$		
$\text{Ca}_3\text{N}_2$	Irreducible representations	$E_u$	$A_u$	$E$	$E_u$	$A_{1g}$	$B_u$	$A_1$	$A_{1g}$		
$\text{Ba}_3\text{P}_2$		$E_u$	$A_u$	$A_2$	$E_u$	$A_{1g}$	$A_g$	$A_1$	$A_{1g}$		
$\text{Ba}_3\text{As}_2$		$E_u$	$A_u$	$A_2$	$E_u$	$A_{1g}$	$A_g$	$A_1$	$A_{1g}$		

TABLE V. The calculated effective mass ( $m^*$ ), elastic constant ( $C$ ), DP constant ( $E_1$ ), electron mobility ( $\mu$ ), and relaxation time ( $\tau$ ) along  $x$  direction and  $y$  direction of monolayer  $\text{Ca}_3\text{N}_2$ ,  $\text{Ba}_3\text{P}_2$ , and  $\text{Ba}_3\text{As}_2$ .

Material	$m_x^*$ ( $m_e$ )	$m_y^*$ ( $m_e$ )	$E_{1x}$ (eV)	$E_{1y}$ (eV)	$C_{2D-x}$ (N/m)	$C_{2D-y}$ (N/m)	$\mu_x$ ( $\text{cm}^2 \text{V}^{-1} \text{s}^{-1}$ )	$\mu_y$ ( $\text{cm}^2 \text{V}^{-1} \text{s}^{-1}$ )	$\tau_x$ (fs)	$\tau_y$ (fs)
$\text{Ca}_3\text{N}_2$	0.36	0.36	1.66	1.68	82.5567	82.6171	$3.30 \times 10^3$	$3.22 \times 10^3$	665.20	649.93
$\text{Ba}_3\text{P}_2$	0.375	0.375	1.007	1.013	35.7886	35.6856	$3.58 \times 10^3$	$3.53 \times 10^3$	752.268	741.243
$\text{Ba}_3\text{As}_2$	0.32	0.32	0.575	0.579	32.5165	32.4138	$1.37 \times 10^4$	$1.35 \times 10^4$	$2.46 \times 10^3$	$2.42 \times 10^3$

While definitive accuracy requires experimental validation, this discrepancy does not undermine the validity of our analysis focused on optical absorption characteristics in the current study.

It can be observed that all three materials have their optical absorption edges in the IR region. Their absorption range extends from the IR to the deep UV region. These materials demonstrate a high optical absorption coefficient, approximately  $10^4 \text{ cm}^{-1}$  in the IR, visible (VIS), and UV regions. This is comparable with organic perovskite solar cells [69]. Furthermore, their optical absorption characteristics display isotropic properties in different in-plane directions.

Furthermore, it is essential to consider the effect of the exciton on the optical properties of 2D indirect band-gap semiconductors. The lowest energy exciton's binding energy is calculated in this study by finding the difference between the QP band-gap energy, which is a minimal direct gap determined by the  $G_0W_0$  method, and the exciton energy, which is the energy of the lowest transition in the optical spectrum obtained through the  $G_0W_0+BSE$  method. Our calculations show that  $\text{Ca}_3\text{N}_2$  has a first optical absorption peak at the photon energy of 0.17 eV,  $\text{Ba}_3\text{P}_2$  has one at 0.38 eV, and  $\text{Ba}_3\text{As}_2$  has one at 0.41 eV. This excitonic peak in the IR range is located below the calculated  $G_0W_0$  band gap of 0.66 eV for  $\text{Ca}_3\text{N}_2$ , 0.52 eV for  $\text{Ba}_3\text{P}_2$ , and 0.57 eV for  $\text{Ba}_3\text{As}_2$ . We estimate the binding energy of the first exciton to be 0.49 eV for  $\text{Ca}_3\text{N}_2$ , 0.14 eV for  $\text{Ba}_3\text{P}_2$ , and 0.16 eV for  $\text{Ba}_3\text{As}_2$ .

It is worth noting that monolayer  $\text{II}_3\text{V}_2$  compounds have a higher exciton-binding energy compared to bulk materials like silicon, which only has an exciton-binding energy of 15 meV [70]. This is due to the quantum confinement effect that results from changes in dimensionality, which alters the wave functions of electrons and holes and enhances their interaction, reducing the screening effect of electrons. When compared to other common 2D materials like TMDs, graphene derivatives, IV/III–V compounds, black phosphorus, and functionalized MXenes, monolayer  $\text{II}_3\text{V}_2$  compounds exhibit a relatively smaller exciton-binding energy that is comparable to that of narrow-gap 2D materials like  $\text{TiS}_3$ ,  $\text{Ti}_2\text{CO}_2$ , and topological materials like Sn, SnF, PbTe, single-quintuple layer  $\text{Bi}_2\text{Se}_3$ , and  $\text{GaBiCl}_2$  [71,72].

The above studies show a linear scaling law between the quasiparticle band gap ( $E_g$ ) and the exciton-binding energy ( $E_b$ ) of 2D semiconductors, regardless of their lattice configuration, bonding characteristics, and topological properties [71,72]. Therefore, the smaller exciton-binding energy of monolayer  $\text{II}_3\text{V}_2$  compounds compared to other 2D materials is primarily due to the narrow band gap of  $\text{II}_3\text{V}_2$ . This implies that monolayer  $\text{II}_3\text{V}_2$  compounds have enough charge carriers for the reaction process, enabling effective electron-hole pair separation. As a result,  $\text{II}_3\text{V}_2$  monolayers are promising candidates for various applications with their isotropic optical response, broad photoresponse range, ideal IR absorption, and high optical absorption coefficient.

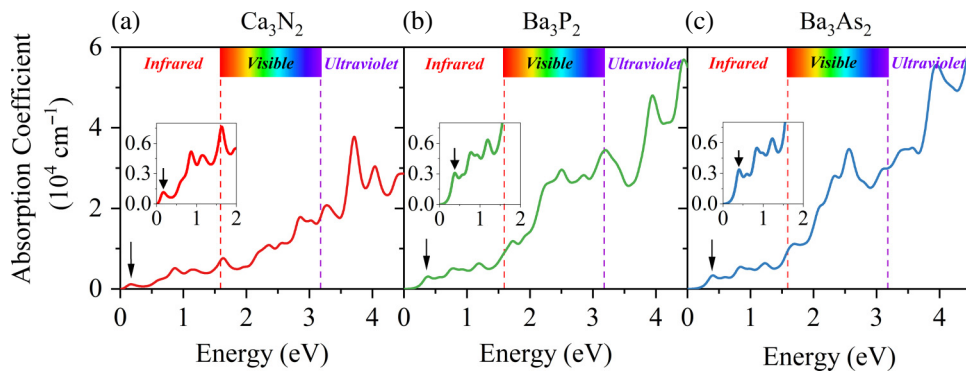


FIG. 9. The optical absorption coefficients for the monolayer  $\text{Ca}_3\text{N}_2$ ,  $\text{Ba}_3\text{P}_2$ , and  $\text{Ba}_3\text{As}_2$  using the  $G_0W_0+BSE$  method (a)–(c). The first optical absorption peak in the IR range is specifically enlarged, labeled, and inserted in panels (a)–(c).

#### IV. CONCLUSION

In this study, we utilized first-principles calculations to design and analyze three alternative binary monolayer narrow-gap semiconductors:  $\text{Ca}_3\text{N}_2$ ,  $\text{Ba}_3\text{P}_2$ , and  $\text{Ba}_3\text{As}_2$ , composed of group II-V elements with a 3:2 stoichiometry and belonging to the  $P\bar{3}m1$  space group. We exhaustively investigate their structural, mechanical, electronic, and optical properties. These materials exhibit remarkable energetic, mechanical, dynamic, and thermal stability alongside isotropic mechanical behavior characterized by excellent in-plane stiffness and flexibility. Furthermore, as indirect narrow-gap semiconductors with high electron mobilities and significant light absorption across the IR to deep UV spectrum, and coupled with lower exciton-binding energies than other common 2D materials, these other materials demonstrate promising potential for applications in a wide range of modern photoelectronic fields, including IR detection, ambipolar transistors, medical imaging, optical communication, and more, highlighting their significant applicability and potential impact on future technological advancements in photoelectric devices and systems.

#### ACKNOWLEDGMENTS

This research was funded by the National Natural Science Foundation of China (Grant No. 12164050), the Major Science and Technology Project of Precious Metal Materials Genetic Engineering in Yunnan Province (Grants No. 2019ZE001-1, No. 202002AB080001-6, and No. 2018IC058), and the Program for Yunling Scholars in Yunnan Province, Program for Donglu Scholars in Yunnan University, Scientific Research Fund Project of Yunnan Provincial Education Department (Grant No. 2024Y747), the Yunnan Fundamental Research Projects (Grants No. 202201AU070019 and No. 202201AU070036), the Introduction of Talents Projects (Grant No. XJ20210018), the Special Basic Cooperative Research Programs of Yunnan Provincial Undergraduate Universities (Grants No. 202101BA070001-162 and No. 202101BA070001-175), the Program for Frontier Research Team of Kunming University 2023.

- 
- [1] J. Zha, M. Luo, M. Ye, T. Ahmed, X. Yu, D. Lien, Q. He, D. Lei, J. C. Ho, J. Bullock, K. B. Crozier, and C. Tan, Infrared photodetectors based on 2D materials and nanophotonics, *Adv. Funct. Mater.* **32**, 2111970 (2021).
  - [2] N. Huo, S. Gupta, and G. Konstantatos,  $\text{MoS}_2$ -HgTe quantum dot hybrid photodetectors beyond 2  $\mu\text{m}$ , *Adv. Mater.* **29**, 1606576 (2017).
  - [3] F. Wang, Y. Zhang, Y. Gao, P. Luo, J. Su, W. Han, K. Liu, H. Li, and T. Zhai, 2D metal chalcogenides for IR photodetection, *Small* **15**, 1901347 (2019).

- [4] Y. Fang, Y. Ge, C. Wang, and H. Zhang, Mid-infrared photonics using 2D materials: Status and challenges, *Laser Photonics Rev.* **14**, 1900098 (2020).
- [5] L.-H. Zeng, M.-Z. Wang, H. Hu, B. Nie, Y.-Q. Yu, C.-Y. Wu, L. Wang, J.-G. Hu, C. Xie, F.-X. Liang, and L.-B. Luo, Monolayer graphene/germanium Schottky junction as high-performance self-driven infrared light photodetector, *ACS Appl. Mater. Interfaces* **5**, 9362 (2013).
- [6] C. Yin, C. Gong, J. Chu, X. Wang, C. Yan, S. Qian, Y. Wang, G. Rao, H. Wang, Y. Liu, X. Wang, J. Wang, W. Hu, C. Li, and J. Xiong, Ultrabroadband photodetectors up to 10.6  $\mu\text{m}$  based on 2D  $\text{Fe}_3\text{O}_4$  nanosheets, *Adv. Mater.* **32**, 2002237 (2020).
- [7] G. Rao, X. Wang, Y. Wang, P. Wangyang, C. Yan, J. Chu, L. Xue, C. Gong, J. Huang, J. Xiong, and Y. Li, Two-dimensional heterostructure promoted infrared photodetection devices, *InfoMat* **1**, 272 (2019).
- [8] J. Bullock, M. Amani, K. Xu, H. K. Tsang, and J.-B. Xu, High-responsivity graphene/silicon-heterostructure waveguide photodetectors, *Nat. Photonics* **7**, 888 (2013).
- [9] X. Wang, Z. Cheng, J. Cho, Y.-Z. Chen, G. H. Ahn, V. Adinolfi, V. R. Shrestha, Y. Gao, K. B. Crozier, Y.-L. Chueh, and A. Javey, Polarization-resolved black phosphorus/molybdenum disulfide mid-wave infrared photodiodes with high detectivity at room temperature, *Nat. Photonics* **12**, 601 (2018).
- [10] L.-B. Luo, Y.-F. Zou, C.-W. Ge, K. Zheng, D.-D. Wang, R. Lu, T.-F. Zhang, Y.-Q. Yu, and Z.-Y. Guo, A surface plasmon enhanced near-infrared nanophotodetector, *Adv. Opt. Mater.* **4**, 763 (2016).
- [11] L. Huang, B. Dong, X. Guo, Y. Chang, N. Chen, X. Huang, W. Liao, C. Zhu, H. Wang, C. Lee, and K.-W. Ang, Waveguide-integrated black phosphorus photodetector for mid-infrared applications, *ACS Nano* **13**, 913 (2019).
- [12] E. Wu, D. Wu, C. Jia, Y. Wang, H. Yuan, L. Zeng, T. Xu, Z. Shi, Y. Tian, and X. Li, In situ fabrication of 2D  $\text{WS}_2$ /Si type-II heterojunction for self-powered broadband photodetector with response up to mid-infrared, *ACS Photonics* **6**, 565 (2019).
- [13] C.-H. Liu, Y.-C. Chang, T. B. Norris, and Z. Zhong, Graphene photodetectors with ultra-broadband and high responsivity at room temperature, *Nat. Nanotechnol.* **9**, 273 (2014).
- [14] J. An, B. Wang, C. Shu, W. Wu, B. Sun, Z. Zhang, D. Li, and S. Li, Research development of 2D materials based photodetectors towards mid-infrared regime, *Nano Select* **2**, 527 (2020).
- [15] J. Yin, Z. Tan, H. Hong, J. Wu, H. Yuan, Y. Liu, C. Chen, C. Tan, F. Yao, T. Li, Y. Chen, Z. Liu, K. Liu, and H. Peng, Ultrafast and highly sensitive infrared photodetectors based on two-dimensional oxyselenide crystals, *Nat. Commun.* **9**, 3311 (2018).
- [16] M. Long, Y. Wang, P. Wang, X. Zhou, H. Xia, C. Luo, S. Huang, G. Zhang, H. Yan, Z. Fan, X. Wu, X. Chen, W. Lu, and W. Hu, Palladium diselenide long-wavelength infrared photodetector with high sensitivity and stability, *ACS Nano* **13**, 2511 (2019).
- [17] M. Amani, C. Tan, G. Zhang, C. Zhao, J. Bullock, X. Song, H. Kim, V. R. Shrestha, Y. Gao, K. B. Crozier, M.

- Scott, and A. Javey, Solution-synthesized high-mobility tellurium nanoflakes for short-wave infrared photodetectors, *ACS Nano* **12**, 7253 (2018).
- [18] L. Ye, H. Li, Z. Chen, and J. Xu, Near-infrared photodetector based on  $\text{MoS}_2$ /black phosphorus heterojunction, *ACS Photonics* **3**, 692 (2016).
- [19] M. Long, A. Gao, P. Wang, H. Xia, C. Ott, C. Pan, Y. Fu, E. Liu, X. Chen, W. Lu, T. Nilges, J. Xu, X. Wang, W. Hu, and F. Miao, Room temperature high-detectivity mid-infrared photodetectors based on black arsenic phosphorus, *Sci. Adv.* **3**, e1700589 (2017).
- [20] A. Gupta, T. Sakthivel, and S. Seal, Recent development in 2D materials beyond graphene, *Prog. Mater. Sci.* **73**, 44 (2015).
- [21] M. Ye, D. Zhang, and Y. Yap, Recent advances in electronic and optoelectronic devices based on two-dimensional transition metal dichalcogenides, *Electronics* **6**, 43 (2017).
- [22] J. Chen, Q. Huang, H. Huang, L. Mao, M. Liu, X. Zhang, and Y. Wei, Recent progress and advances in the environmental applications of MXene related materials, *Nanoscale* **12**, 3574 (2020).
- [23] S. Kang, D. Lee, J. Kim, A. Capasso, H. S. Kang, J.-W. Park, C.-H. Lee, and G.-H. Lee, 2D semiconducting materials for electronic and optoelectronic applications: Potential and challenge, *2D Mater.* **7**, 022003 (2020).
- [24] W. Liu, M. Liu, X. Liu, X. Wang, H. Deng, M. Lei, Z. Wei, and Z. Wei, Recent advances of 2D materials in nonlinear photonics and fiber lasers, *Adv. Opt. Mater.* **8**, 1901631 (2020).
- [25] J. You, Y. Zhao, L. Wang, and W. Bao, Recent developments in the photocatalytic applications of covalent organic frameworks: A review, *J. Clean. Prod.* **291**, 125822 (2021).
- [26] M. Long, P. Wang, H. Fang, and W. Hu, Progress, challenges, and opportunities for 2D material based photodetectors, *Adv. Funct. Mater.* **29**, 1803807 (2019).
- [27] J. Cheng, C. Wang, X. Zou, and L. Liao, Recent advances in optoelectronic devices based on 2D materials and their heterostructures, *Adv. Opt. Mater.* **7**, 1800441 (2019).
- [28] N. Huo and G. Konstantatos, Recent progress and future prospects of 2D-based photodetectors, *Adv. Mater.* **30**, 1801164 (2018).
- [29] F. Xia, H. Wang, D. Xiao, M. Dubey, and A. Ramasubramanian, Two-dimensional material nanophotonics, *Nat. Photonics* **8**, 899 (2014).
- [30] A. K. Geim and I. V. Grigorieva, van der Waals heterostructures, *Nature* **499**, 419 (2013).
- [31] M. Zhao, W. Xia, Y. Wang, M. Luo, Z. Tian, Y. Guo, W. Hu, and J. Xue,  $\text{Nb}_2\text{SiTe}_4$ : A stable narrow-gap two-dimensional material with ambipolar transport and mid-infrared response, *ACS Nano* **13**, 10705 (2019).
- [32] Z. Azarmi, M. Naseri, and S. Parsamehr, Penta- $\text{BeP}_2$  monolayer: A new 2D beryllium phosphate with a narrow band gap, *Chem. Phys. Lett.* **728**, 136 (2019).
- [33] X.-F. Sheng, X.-X. Rao, C. Ke, and W.-B. Kang, 2D plane XP2 ( $X = \text{Ni}, \text{Pd}, \text{Pt}$ ) with narrow band gaps, ultrahigh carrier mobility and high electrical transport performance, *Appl. Surf. Sci.* **601**, 154166 (2022).
- [34] N. Lu, Z. Zhuo, H. Guo, P. Wu, W. Fa, X. Wu, and X. C. Zeng,  $\text{CaP}_3$ : A new two-dimensional functional material with desirable band gap and ultrahigh carrier mobility, *J. Phys. Chem. Lett.* **9**, 1728 (2018).
- [35] W. Xu, R. Wang, Y. Jin, X. Wu, and H. Xu, New family of two-dimensional group-( $\text{II}_3-\text{V}_2$ ) photoelectric materials, *J. Phys. Chem. C* **123**, 16851 (2019).
- [36] Q. Xu, R. Yu, Z. Fang, X. Dai, and H. Weng, Topological nodal line semimetals in the  $\text{CaP}_3$  family of materials, *Phys. Rev. B* **95**, 045136 (2017).
- [37] P. Tang, J.-H. Yuan, Y.-Q. Song, M. Xu, K.-H. Xue, and X.-S. Miao,  $\text{BaAs}_3$ : A narrow gap 2D semiconductor with vacancy-induced semiconductor–metal transition from first principles, *J. Mater. Sci.* **54**, 12676 (2019).
- [38] Z. Li, M. Qian, H. Zhao, D. Zhang, B. Chen, H. Qiu, and T. Zhang, Defect-induced diverse electronic, magnetic and optical properties in monolayer  $\text{CaP}_3$ , *Mater. Today Commun.* **23**, 100925 (2020).
- [39] M. Laurien, H. Saini, and O. Rubel, Band alignment of monolayer  $\text{CaP}_3$ ,  $\text{CaAs}_3$ ,  $\text{BaAs}_3$  and the role of  $p$ - $d$  orbital interactions in the formation of conduction band minima, *Phys. Chem. Chem. Phys.* **23**, 7418 (2021).
- [40] X.-L. Zhu, P.-F. Liu, Y.-Y. Wu, P. Zhang, G. Xie, and B.-T. Wang, Significant enhancement of the thermoelectric properties of  $\text{CaP}_3$  through reducing the dimensionality, *Mater. Adv.* **1**, 3322 (2020).
- [41] G. Kresse and J. Furthmüller, Efficient iterative schemes for ab initio total-energy calculations using a plane-wave basis set, *Phys. Rev. B Condens. Matter* **54**, 11169 (1996).
- [42] G. Kresse and D. Joubert, From ultrasoft pseudopotentials to the projector augmented-wave method, *Phys. Rev. B* **59**, 1758 (1999).
- [43] P. E. Blochl, Projector augmented-wave method, *Phys. Rev. B Condens. Matter* **50**, 17953 (1994).
- [44] J. P. Perdew, K. Burke, and M. Ernzerhof, Generalized gradient approximation made simple, *Phys. Rev. Lett.* **77**, 3865 (1996).
- [45] J. Heyd, G. E. Scuseria, and M. Ernzerhof, Hybrid functionals based on a screened Coulomb potential, *J. Chem. Phys.* **118**, 8207 (2003).
- [46] J. Heyd and G. E. Scuseria, Efficient hybrid density functional calculations in solids: Assessment of the Heyd-Scuseria-Ernzerhof screened Coulomb hybrid functional, *J. Chem. Phys.* **121**, 1187 (2004).
- [47] M. Shishkin and G. Kresse, Implementation and performance of the frequency-dependent  $GW$  method within the PAW framework, *Phys. Rev. B* **74**, 035101 (2006).
- [48] F. Karlický and M. Otyepka, Band gaps and optical spectra of chlorographene, fluorographene and graphane from  $\text{G}_0\text{W}_0$ ,  $\text{GW}_0$  and  $GW$  calculations on top of PBE and HSE06 orbitals, *J. Chem. Theory Comput.* **9**, 4155 (2013).
- [49] L. Chaput, A. Togo, I. Tanaka, and G. Hug, Phonon-phonon interactions in transition metals, *Phys. Rev. B* **84**, 094302 (2011).
- [50] P. Giannozzi *et al.*, QUANTUM ESPRESSO: A modular and open-source software project for quantum simulations of materials, *J. Phys.: Condens. Matter* **21**, 395502 (2009).
- [51] C. S. Jung, D. Kim, S. Cha, Y. Myung, F. Shojaei, H. G. Abbas, J. A. Lee, E. H. Cha, J. Park, and H. S. Kang, Two-dimensional GeAs with a visible range band gap, *J. Mater. Chem. A* **6**, 9089 (2018).

- [52] Y. Li, Y. Liao, and Z. Chen, Be<sub>2</sub>C monolayer with quasi-planar hexacoordinate carbons: A global minimum structure, *Angew. Chem. Int. Ed.* **53**, 7248 (2014).
- [53] M. Born and K. Huang, *Dynamical Theory of Crystal Lattices* (Oxford University Press, Oxford, 1954).
- [54] E. Cadelano, P. L. Palla, S. Giordano, and L. Colombo, Elastic properties of hydrogenated graphene, *Phys. Rev. B* **82**, 235414 (2010).
- [55] T. Li, J. W. Morris, N. Nagasako, S. Kuramoto, and D. C. Chrzan, “Ideal” engineering alloys, *Phys. Rev. Lett.* **98**, 105503 (2007).
- [56] W. Meng, X. Wang, Z. Xiao, J. Wang, D. B. Mitzi, and Y. Yan, Parity-forbidden transitions and their impact on the optical absorption properties of lead-free metal halide perovskites and double perovskites, *J. Phys. Chem. Lett.* **8**, 2999 (2017).
- [57] X. Nie, S. H. Wei, and S. B. Zhang, Bipolar doping and band-gap anomalies in delafossite transparent conductive oxides, *Phys. Rev. Lett.* **88**, 066405 (2002).
- [58] K.-L. Zhang, C.-M. Liu, F.-Q. Huang, C. Zheng, and W.-D. Wang, Study of the electronic structure and photocatalytic activity of the biocI photocatalyst, *Appl. Catal. B: Environ.* **68**, 125 (2006).
- [59] X. Zhang, B. Li, J. Wang, Y. Yuan, Q. Zhang, Z. Gao, L. M. Liu, and L. Chen, The stabilities and electronic structures of single-layer bismuth oxyhalides for photocatalytic water splitting, *Phys. Chem. Chem. Phys.* **16**, 25854 (2014).
- [60] M. Abboud, D. H. Ozbey, M. E. Kilic, and E. Durgun, Investigation of anisotropic mechanical, electronic, and charge carrier transport properties of germanium-pnictogen monolayers, *J. Phys. D: Appl. Phys.* **55**, 185302 (2022).
- [61] B. Silvi and A. Savin, Classification of chemical bonds based on topological analysis of electron localization functions, *Nature* **371**, 683 (1994).
- [62] R. J. Clements, J. C. Womack, and C. K. Skylaris, Electron localisation descriptors in ONETEP: A tool for interpreting localisation and bonding in large-scale DFT calculations, *Electron. Struct.* **2**, 027001 (2020).
- [63] A. Savin, O. Jepsen, J. Flad, O. K. Andersen, H. Preuss, and H. G. von Schnering, Electron localization in solid-state structures of the elements: The diamond structure, *Angew. Chem. Int. Ed. in English* **31**, 187 (1992).
- [64] N. Wang, M. Li, H. Xiao, H. Gong, Z. Liu, X. Zu, and L. Qiao, Optimizing the thermoelectric transport properties of Bi<sub>2</sub>O<sub>2</sub>Se monolayer via biaxial strain, *Phys. Chem. Chem. Phys.* **21**, 15097 (2019).
- [65] F. Q. Wang, Y. Guo, Q. Wang, Y. Kawazoe, and P. Jena, Exceptional thermoelectric properties of layered GeAs<sub>2</sub>, *Chem. Mater.* **29**, 9300 (2017).
- [66] Y. Pei, X. Shi, A. LaLonde, H. Wang, L. Chen, and G. J. Snyder, Convergence of electronic bands for high performance bulk thermoelectrics, *Nature* **473**, 66 (2011).
- [67] E. E. Salpeter and H. A. Bethe, A relativistic equation for bound-state problems, *Phys. Rev.* **84**, 1232 (1951).
- [68] M. Gajdos, K. Hummer, G. Kresse, J. Furthmüller, and F. Bechstedt, Linear optical properties in the projector-augmented wave methodology, *Phys. Rev. B* **73**, 045112 (2006).
- [69] M. Shirayama, H. Kadowaki, T. Miyadera, T. Sugita, M. Tamakoshi, M. Kato, T. Fujiseki, D. Murata, S. Hara, T. N. Murakami, S. Fujimoto, M. Chikamatsu, and H. Fujiwara, Optical transitions in hybrid perovskite solar cells: Ellipsometry, density functional theory, and quantum efficiency analyses for CH<sub>3</sub>NH<sub>3</sub>PbI<sub>3</sub>, *Phys. Rev. Appl.* **5**, 014012 (2016).
- [70] L. Yang, C. D. Spataru, S. G. Louie, and M. Y. Chou, Enhanced electron-hole interaction and optical absorption in a silicon nanowire, *Phys. Rev. B* **75**, 201304 (2007).
- [71] Z. Jiang, Z. Liu, Y. Li, and W. Duan, Scaling universality between band gap and exciton binding energy of two-dimensional semiconductors, *Phys. Rev. Lett.* **118**, 266401 (2017).
- [72] J.-H. Choi, P. Cui, H. Lan, and Z. Zhang, Linear scaling of the exciton binding energy versus the band gap of two-dimensional materials, *Phys. Rev. Lett.* **115**, 066403 (2015).